HF MIMO NVIS Measurements with Co-located Dipoles for Future Tactical Communications

Robert C. Daniels, Steven W. Peters, and Robert W. Heath, Jr.

***Abstract*—Multiple antennas in transceivers can increase system spectral efficiency, reduce transmit power, enable robustness to interference, and increase overall reliability through multiple-input multiple-output processing (MIMO). Consequently, high frequency (HF) networks, which feature extreme spectrum scarcity and unreliability, are prime for MIMO exploitation. Unfortunately, the desired antenna spacing for MIMO is proportional to the wavelength (tens of meters at HF). One promising approach is to utilize two antennas in a single antenna footprint through cross-polarization. This configuration has not yet been fully validated for MIMO at HF. In this paper, we demonstrate MIMO capabilities in near vertical incidence sky-wave (NVIS) propagation through a measurement campaign. This paper shows that MIMO is a game changer for HF NVIS with up to $2.27\times$ data rate gains, up to $9\times$ less transmit power, and $> 3\times$ fewer link failures. This paper also provides critical channel metrics for baseband designers of future MIMO HF protocols as demonstrated in our companion paper [1].**

I. Introduction

Tactical links, in part, provide the Warfighter with information superiority. When operating in remote locations without communications infrastructure or a clear view of a satellite, high frequency (HF) radios leverage sky-wave signal propagation to maintain connectivity. Currently, HF data rates are prohibitively low, making transmission of large images or video infeasible. The defense industry has increased HF data rates over the past decade through wider bandwidths in conjunction with spectrally efficient waveforms (e.g., higher-order constellations and efficient forward error correction). This work has resulted in higher data rates, but only in extremely high signal-to-noise ratio (SNR) conditions [2]. These conditions are not consistently observed due to the variability of the HF channel; this is especially true in near-vertical incidence sky-wave (NVIS) conditions. Further, expanding rates through bandwidth expansion has become increasingly difficult due to the scarcity of acquirable HF spectrum.

If feasible and practical, multiple-input multiple-output (MIMO) HF tactical communications is a game changer. In commercial networks MIMO has multiplied data rates, enabled robustness to interference, increased link reliability, and decimated radio energy consumption [3]. Consequently, MIMO HF NVIS feasibility provides substantial impact. While academic and commercial research has suggested that HF sky-wave channels can support MIMO processing [4], prior MIMO HF NVIS measurements have made impractical assumptions for tactical communications [5], [6]. For example, prior work has assumed antenna separation of many wavelengths (tens of meters) at either the transmitter or receiver; a flexible solution cannot afford this. Further, HF measurement campaigns failed to provide many MIMO metrics for simulation and design.

Supported in part by Office of Naval Research contract N00014-12-M-0232.
Dr. Daniels, Dr. Peters, and Dr. Heath are with Kuma Signals, LLC, 3520 Exec. Center Dr, Ste 120, Austin, TX, 78731. Dr. Heath is also with The University of Texas at Austin (UT). The terms of this arrangement have been reviewed and approved by UT in accordance with its objective research policy.

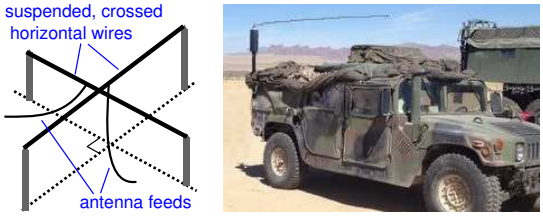

Fig. 1. Cross-polarized horizontal sky-wave antennas (*left*). Sky-wave antenna on vehicle (*right*, compact configuration requires exotic antennas). Image copied with permission from `www.hi-q-militaryantennas.com`.

Future MIMO HF systems will exploit both diversity and spatial multiplexing through smart adaptive processing. In diversity mode, links exploit channel variability between different antennas to improve signal quality. For example, one simple diversity algorithm selects the transmit-receive antenna pair with the best SNR. In spatial multiplexing mode, each transmit antenna radiates a different waveform containing independent data to multiply data rates. Because the wireless channel mixes each of these waveforms, the receiver must separate them. This cannot occur, however, if the propagation between each transmit and receive antenna is the same. It is therefore necessary to demonstrate the ability of the propagation medium to support both MIMO modes.

This paper demonstrates practical MIMO NVIS feasibility through measurements with 2 co-located, horizontally-oriented dipole antennas at perpendicular polarizations for both the transmitter and receiver (a 2×2 MIMO configuration). Co-located, cross-polarized antennas embody a practical tactical MIMO HF implementation, as illustrated in Figure 1. This cross-polarized configuration has also been exploited by commercial UHF communication systems [7]. The measurements reported in this paper show that 2.27 times larger data rates, 9 times less transmit power, and > 3 times fewer link failures were observed in 2×2 MIMO HF NVIS channels with cross-polarized antennas by exploiting both diversity *and* spatial multiplexing. This paper also provides critical channel parameters, including spatial correlation, for baseband designers to benchmark performance and design MIMO HF protocols [1].

II. System Model & Background

This paper only considers narrowband channel responses through an 800 Hz measurement bandwidth. Measurements will not be able to separate signal components from multiple ionospheric reflections (including ordinary and extraordinary waves). Nevertheless, the aggregate measurement will characterize the ability of the HF MIMO NVIS channel to support

978-0-7695-5124-1/13 $31.00 © 2013 IEEE
DOI 10.1109/MILCOM.2013.210

IEEE computer society

Fig. 2. Sketch of the MFJ-17758 dipole antenna. Loading coils both enable the antenna to operate in both the 80 m and 40 m bands without changing the antenna configuration and shorten the antenna for 80 m operation. Antenna length is 85 feet (standard half-wave antenna at 80 m would be 131 ft in length).

MIMO communications since this narrowband feasibility also (implicitly) depends on the path differences in reflections.

This paper models channels through a discrete-time complex baseband system, as enabled by the transmit and receive hardware. Let n be the discrete time index representing n/f_r seconds and let $\mathbf{x}[n] \in \mathbb{C}^{2\times 1}$ represent the two complex baseband probing signal samples transmitted on transmit antennas, TX 1 and TX 2, respectively. Simultaneously, the receiver captures $\mathbf{y}[n] \in \mathbb{C}^{2\times 1}$ on each of its receive antennas, RX 1 and RX 2, respectively. The receive antennas are subject to independent additive complex zero-mean Gaussian random processes with vector $\mathbf{v}[n] \in \mathbb{C}^{2\times 1}$ providing noise samples at time index n such that σ_1^2, σ_2^2 represents the noise power on RX 1 and RX 2, respectively. Assuming a narrowband response (no delay spread), the system model provides the relationship

$$\mathbf{y}[n] = \mathbf{H}\mathbf{x}[n] + \mathbf{v}[n] \tag{1}$$

where $\mathbf{H} \in \mathbb{C}^{2\times 2}$ contains all zero-excess-delay impulse response coefficients $h_{i,j} \in \mathbb{C}$ between TX j and RX i.

Consider the singular value decomposition of $\mathbf{H} = \mathbf{U}\mathbf{S}\mathbf{V}^H$ where $\mathbf{S} = \text{diag}\{s_{\text{max}}, s_{\text{min}}\}$ is a diagonal matrix with singular values on its diagonal, s_{max} and s_{min}, $s_{\text{max}} > s_{\text{min}}$. Note the relationship $\mathbf{U}^H\mathbf{H}\mathbf{V}\mathbf{x}[n] + \mathbf{v}[n] = \mathbf{S}\mathbf{x}[n] + \mathbf{v}[n]$ which shows that, with specific precoding at the transmitter (SVD precoding) and a specific equalizer at the receiver, the SNR becomes $s_{\text{max}}^2/\sigma_1^2$ or $s_{\text{min}}^2/\sigma_2^2$ for the data transmitted on TX 1 or TX 2, respectively. Hence, if independent data is transmitted from TX 1 and TX 2, respectively (as through spatial multiplexing), two independent and parallel links are observed from a single radio, each with their own SNR. If equal power is allocated to each transmit antenna, this configuration is optimal [8]. Assuming fixed Frobenius norm (equivalently, $s_{\text{max}}^2 + s_{\text{min}}^2$ is fixed), the ability of a channel matrix to provide spatial multiplexing is maximized when the ratio of the singular values (also known as the condition number) is 1, i.e., $\kappa(\mathbf{H}) = s_{\text{max}}/s_{\text{min}} = 1$ [9]. In diversity mode, only a single data stream is transmitted, so (ideally) the signal from all transmit-receive pairs may be captured. This yields an improved SNR, namely the **MIMO SNR** $\triangleq \|\mathbf{H}\|_F^2/(\sigma_1^2 + \sigma_2^2)$ where $\|\cdot\|_F$ is the Frobenius norm. It is often useful to provide statistical relationships between the channel matrix elements such that ergodic studies of communication link performance are possible through Monte Carlo simulations [10]. The correlation between the spatial elements is represented through a covariance matrix

$$\mathbf{Q} = \mathbb{E}_{\mathbf{h}}\left[\begin{bmatrix} h_{1,1} & h_{2,1} & h_{1,2} & h_{2,2} \end{bmatrix}^T \times \begin{bmatrix} h_{1,1}^* & h_{2,1}^* & h_{1,2}^* & h_{2,2}^* \end{bmatrix}\right]. \tag{2}$$

III. Channel Measurement Setup

Two primary HF bands are used for NVIS communication: 40 m (frequencies 7.0 to 7.3 MHz) and 80 m (frequencies of 3.5 to 4.0 MHz). Typically, the 40 m band is used during the day when the ionosphere is highly ionized and the 80 m band is used during the night when the D-layer subsides [11]. Measurements in this paper were conducted in the daytime and exploit 40 m single sideband (SSB) communication. All experiments used MFJ-17758 dual-band dipole antennas, horizontally oriented, as illustrated in Figure 2. For effective NVIS operation, horizontal dipoles were suspended with a height of at least 6 feet above ground. This presented challenges for mobile tests and custom antenna mounts (PVC post in cement buckets) were created as illustrated in Figure 3.

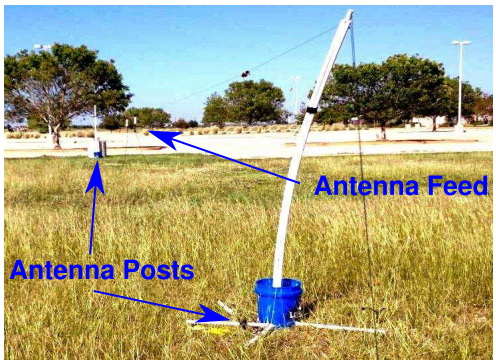

Fig. 3. Picture of RX 2 antenna during measurement.

At the transmitter a stereo WAV file probed the wireless channel. The file was played in a loop through an audio application on a laptop computer. The audio signal was transferred through the sound card of the laptop and separated into left and right channels with a stereo cable splitter. Each of the stereo cables delivered data to a separate HF radio through the microphone connection. The Yaesu FT-757GX II HF radio was used for TX 1 and the ICOM IC-756 HF radio for TX 2). At the receiver, the baseband hardware consisted of two Ettus Research USRP N210 software defined radios (SDRs) with BasicRX daughtercards. The frequency reference of the first receiver (RX 1) drove the frequency reference of the second receiver (RX 2). Because the time-stamp of samples captured on these disparate devices needed to match, a 1 pulse-per-second digital signal was generated by RX 1 and fed into RX 2 to reset the time-stamp counters. Each of the SDRs were connected to the computer through a Gigabit Ethernet port.

Figure 4 shows the custom training sequence that was sent in a loop to enable the receiver to obtain successive channel measurements on each receive antenna. After a buffer at the beginning, N_{SFTU} short frequency training unit sequences (SFTUs) of L_{SFTU} symbols were sent on the first transmit antenna. After the SFTUs were transmitted on TX 1, a buffer allowed TX 2 to transmit its SFTUs. The SFTUs enabled coarse timing (frame synchronization) through self-correlation algorithms. TX 1 and TX 2 followed SFTU transmission with long frequency training units (LFTUs) of length L_{LFTU}

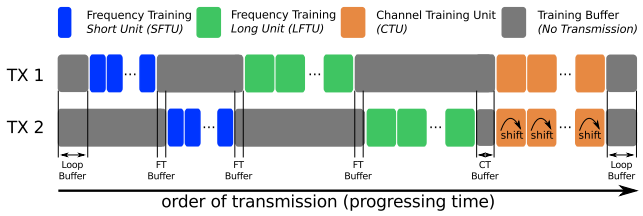

Fig. 4. Probing signal symbol sequence loop for channel measurement.

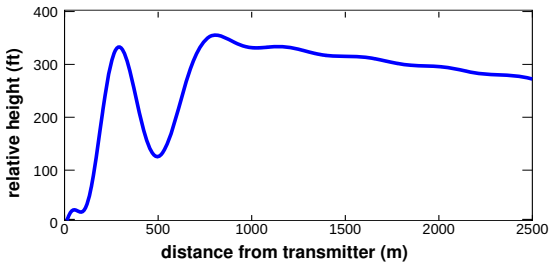

Fig. 5. Smoothed height of terrain for first 2.5 km on geodesic path. The transmitter and receiver are at the same approximate relative height.

with N_{LFTU} repetitions in the same alternating fashion. By exploiting the SFTUs and the LFTUs, the receiver was able to synchronize precisely in frequency and coarsely in time.

Next, channel training units (CTUs) of length L_{CTU} with N_{CTU} repetitions were transmitted concurrently on TX 1 and TX 2. The CTUs (preceded by the blank CT buffer) allowed for fine synchronization and were also used to extract impulse response estimates. To differentiate the CTUs from each transmit antenna, each CTU on TX 2 was cyclically shifted by M symbols. Note that all of the SFTUs, LFTUs, and CTUs were based on Zadoff-Chu sequences. Once the Zadoff Chu symbols were created for the SFTUs, LFTUs, and CTUs, repeated, and then concatenated for each transmit antenna, an audio .WAV file was created in order to generate the training signal for the input to each transmit radio. Then, the symbols were translated to a rate of 44.1 kHz and mapped to left/right audio channels for the samples on TX 1/2, respectively.

Baseband data was sampled at 200 kHz in the receiver and separately passed through a channel select band pass filter for each receive antenna. This is particularly important at HF where significant atmospheric and man-made noise is generated. Next, the SSB data frequency offset, f_d, was removed digitally. This operation was followed by resampling the data to a frequency that is K times larger than f_d ($K \geq 2$). Next, two concurrent signal processing loops were executed, each to determine channel impulse response estimates for TX 1 and TX 2, respectively. The first step used self-reference correlation with max-peak detection to determine the first sample of the first SFTU and the coarse frequency offset estimate. The coarse frequency offset was removed from each received data sample. Another self-reference correlation with the LFTUs refined the frequency offset estimate. After the fine frequency offset was corrected, the data was cross-correlated with the relevant CTU (the unshifted version for the first processing loop, the MK-sample-shifted version for the second processing loop). The peak of this cross-correlation determined the precise CTU sampling point for each transmit antenna and the samples were decimated by a factor K to produce the channel-modified version of the original symbols. Each CTU in both loops was cross correlated $(L_{\text{CTU}} - M)$ times, for each possible distinct cyclic shift of the reference CTU. At the end of this process, up to N_{CTU} multipath profiles with $(L_{\text{CTU}} - M)$ taps were estimated. The channel estimate from the first CTU of the N_{CTU} repetitions were discarded since the first CTU did not preserve cyclic convolution properties [12]. Note that although excess delay taps were estimated, they were insignificant in the data due to the small probing signal bandwidth (800 Hz).

TABLE I. VALUES FOR CHANNEL PROBING WAVEFORM.

Symbol	Value	Description
f_d	680	SSB data offset frequency in Hz
f_r	800	Data symbol rate in Hz
L_{SFTU}	5	SFTU length in symbols
N_{SFTU}	10	SFTU repetitions
L_{LFTU}	51	LFTU length in symbols
N_{LFTU}	2	LFTU repetitions
L_{CTU}	53	CTU length in symbols
N_{CTU}	11	CTU repetitions
L_{FLB}	50	Front Loop Buffer length in symbols
L_{BLB}	30	Back Loop Buffer length in symbols
L_{FTB}	10	FT Buffer length in symbols
L_{CTB}	30	CT Buffer length in symbols
M	27	Shift on each TX 2 CTU in symbols
K	10	Symbol oversample rate for processing

IV. MEASUREMENT LOCATION FOR NVIS ISOLATION

The transmitter and the receiver were separated by a geodesic distance of 19.7 km. Both locations were in public parks on the west side (transmitter) and the northeast side (receiver) of Austin, TX. TX 1 was oriented north-south, TX 2 east-west, RX 1 east-west, and RX 2 north-south. Measurements were conducted from approximately 12:30 PM to 3:30 PM on October 19th, 2012. Table II shows static contributions to the link budget used for measurements in this report. The acceptable loss in the combination of the transmit antenna, receive antenna, and propagation channel is 186 dB.

A *space wave* travels between a transmitter and receiver without interacting with the ionosphere. In the experiment it was suppressed by both the weak radiation of the horizontal dipole antennas in low elevation angles and the transmitter terrain which shadowed the line-of-sight path. Figure 5 shows a 2-D model of the geodesic path. The knife edge diffraction model provides an optimistic estimate of space wave path loss due to diffraction. With this model, the 100 m peak at distance 300 m from the transmitter yields $L_{\text{knife-edge}} = -20\log_{10}\left(0.4 - \sqrt{0.1184 - (0.38 - 0.1\nu)^2}\right) = 15.5$ dB with the Fresnel-Kirchoff diffraction parameter $\nu = h\sqrt{\frac{2(d_1+d_2)}{\lambda d_1 d_2}} = 1.26$ where $h = 100$ m, $d_1 = 300$ m, $d_2 = 19400$ m, and $\lambda = 3 \times 10^8$ m/s / 7×10^6 Hz $= 42.9$ m [13]. Additionally, the Friis free space path loss model provides

TABLE II. MAXIMUM ACCEPTABLE LOSS IN CHANNEL + ANTENNA.

Contribution	Value
Transmit Radio Power (50 W)	17 dB
Thermal Noise Power (1 Hz)	(−204 dB)
Bandwidth Noise Factor (1 kHz)	(30 dB)
Required Signal-to-Noise-Ratio	(5 dB)
Maximum Antenna & Propagation Loss	186 dB

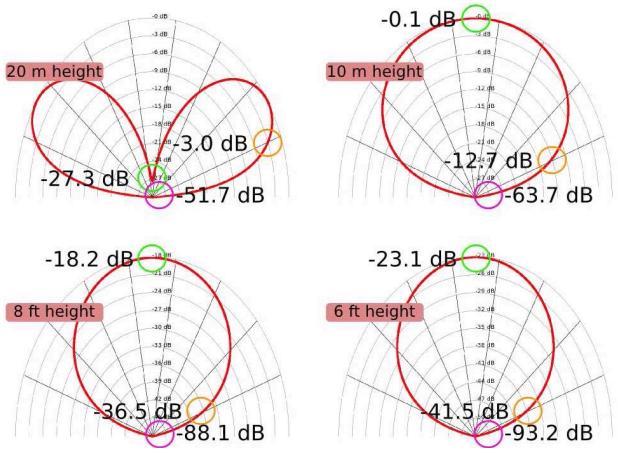

Fig. 6. Radiation patterns as a function of elevation angle at 7 MHz with horizontal half-wave dipole antennas above a perfectly reflecting ground plane at a height of 20 m, 10 m, 2.45 m (8 ft), and 1.83 m (6 ft). Sensitivity is highlighted at elevation angles of 90^o (green), 20^o (orange), and 1^o (magenta).

an optimistic estimate of the loss of the space wave due to electromagnetic wave dispersion. In the experiment this model provided $L_{\text{free-space}} = -20\log_{10}\left(\frac{\lambda}{4\pi d}\right) = 75.2$ dB where $d = d_1 + d_2 = 19700$ m. Figure 6 shows the radiation pattern of the horizontal dipole antenna (computed from (4-116) in [14]) at 7 MHz with variable distance above the ground (the antennas used for measurements in this report were between 6 and 8 feet, depending on sag along the antenna wire). Note that at lower heights, antennas becomes more directional (towards 90^o), but also less sensitive (reduced gain). The elevation angle of the 300 m tall diffraction object (hill) with reference to the transmit antenna was at an elevation angle $< 1^o$ and, with reference to the receive antenna, at an elevation angle $< 20^o$. Hence, the antennas used for the measurements in this report provided, at best, a space wave sensitivity of -36.5 dB and -88.1 dB, at the transmitter and receiver, respectively. Combined, this means that the antenna loss estimate for the space wave was 124.6 dB, well beyond the maximum space-wave antenna loss of $186 - L_{\text{knife-edge}} - L_{\text{free-space}} = 95.3$ dB.

Terrestrial *surface waves* may be used to communicate through current flows, especially at frequencies below 100 MHz and over distances of less than 100 km. Historically, proper modeling of HF surface waves has been the subject of scientific dissonance [15]. Today, it is now understood that surface waves are properly modeled by the theory of Sommerfeld and Norton and only in very small part due to Zenneck waves [15], [16]. Norton defined asymptotic electric field strength approximations (which eliminated complex error function computations) for vertically polarized waves as

$$E_v = 2jI\frac{e^{j(kd-\omega t)}}{d} \times \left(e^{-jkh_1h_2/d} + e^{jkh_1h_2/d}\left(R_v - \frac{(1+R_v)^2(1-R_v)d}{4jk(h_1+h_2)^2}\right)\right)$$

and horizontally polarized waves as

$$E_h = 2jI\sin(\phi)\frac{e^{j(kd-\omega t)}}{d} \times \left(e^{-jkh_1h_2/d} - e^{jkh_1h_2/d}\left(R_h - \frac{(1-R_h)^2(1+R_h)d}{4jk(h_1+h_2)^2}\right)\right)$$

where ϕ is the rotation angle between the transmit and receive antenna, I is the current at the current loop of the antenna, λ is the wavelength of operation, $k = 2\pi/\lambda$ is the wavenumber, f_c is the operating frequency, $\omega = 2\pi f_c$, h_1 is the height at the midpoint of the transmit antenna, h_2 is the height at the midpoint of the receive antenna, d is the propagation distance, R_v is the reflection coefficient of a vertically polarized plane wave with its electric field vector parallel to the plane of incidence, and R_h is the reflection coefficient of a horizontally polarized plane wave with its electric field vector perpendicular to the plane of incidence. Figure 7 shows the surface wave path loss of the experiment through these equations. This result shows the experiment experienced at least 200 dB of surface wave path loss, far exceeding the margin from Table II.

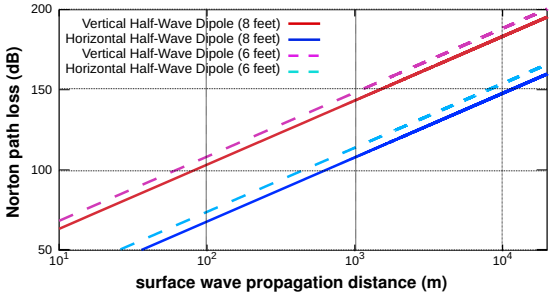

Fig. 7. Path loss of surface waves on a homogeneous Earth with relative permittivity $\epsilon_r = 15$, conductivity $\sigma = 0.01$ S/m, and half-wave antennas. Only horizontal antennas used for measurement.

The remaining propagation phenomenon, *sky waves*, was the only desired communication medium. Several factors influence sky wave propagation including time of day, frequency, and sunspot activity. The VOACAP (Voice of America Coverage Analysis Program for HF Propagation Prediction and Ionospheric Communications Analysis) software package considers all of these factors (and more) to provide an accurate and complex model for ionospheric refraction [17]. On the day of measurement, VOACAP estimated that measurements would observe between 13.8 to 23.6 dB SNR for the antenna configuration. Given this SNR, Monte Carlo simulations reported that the channel estimation process described in Section III would yield estimates, $\hat{\mathbf{H}}$, with normalized mean square error (NMSE) $< 8\times10^{-3}$, where NMSE $\triangleq \mathbb{E}\{\|\mathbf{H}-\hat{\mathbf{H}}\|_F^2/\|\mathbf{H}\|_F^2\}$.

V. Channel Measurement Results and Analysis

HF NVIS channel measurements were captured on October 19th, 2012, 15:06 PM CST at center frequency 7.08806 MHz. In total, fifty-eight (58) 2×2 MIMO channel matrices resulted from training loop probes over a period of 1438 seconds (just under 24 minutes). Figure 8 shows a summary of the statistics for each of the channels. The path energy between all antenna elements varied substantially over the course of the measurement. The instantaneous cross-polarization ratio (XPR) also varied significantly and averaged out to ≈ -2 dB: -2.9 dB for TX 1 -2.0 dB for TX 2. MIMO performance was promising with squared condition numbers that were often very low (implying that the channel is very suitable for spatial multiplexing) and substantially uncorrelated path loss for different transmit-receive paths (advantageous for diversity modes) [18], [19]. Finally, the phase gap between the receive

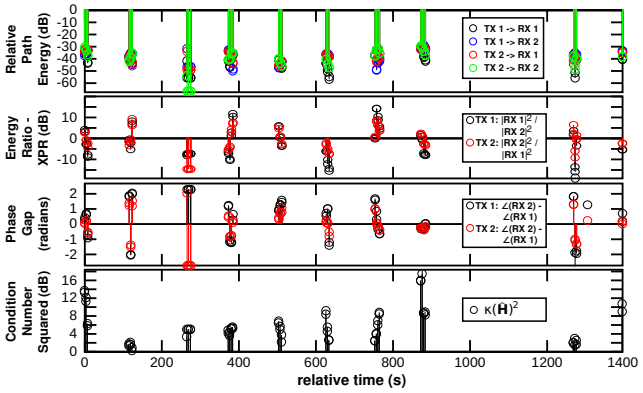
Relative Path Energy (dB)
TX 1 -> RX 1
TX 1 -> RX 2
TX 2 -> RX 1
TX 2 -> RX 2
Energy Ratio - XPR (dB)
TX 1: |RX 1|^2 / |RX 2|^2
TX 2: |RX 2|^2 / |RX 1|^2
Phase Gap (radians)
TX 1: ∠(RX 2) - ∠(RX 1)
TX 2: ∠(RX 2) - ∠(RX 1)
Condition Number Squared (dB)
κ(H)^2
relative time (s)

Fig. 8. Summary of 58 channel measurements on October 19th, 2012.

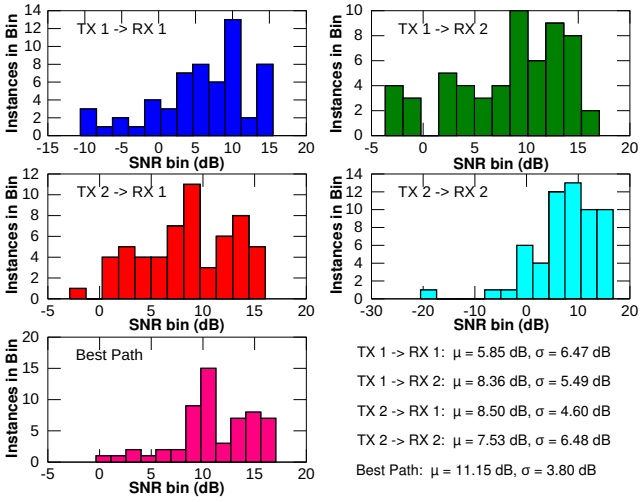
TX 1 -> RX 1
TX 1 -> RX 2
TX 2 -> RX 1
TX 2 -> RX 2
Best Path
Instances in Bin
SNR bin (dB)
TX 1 -> RX 1: μ = 5.85 dB, σ = 6.47 dB
TX 1 -> RX 2: μ = 8.36 dB, σ = 5.49 dB
TX 2 -> RX 1: μ = 8.50 dB, σ = 4.60 dB
TX 2 -> RX 2: μ = 7.53 dB, σ = 6.48 dB
Best Path: μ = 11.15 dB, σ = 3.80 dB

Fig. 9. Histogram of the SNR for all transmit-receive paths. Empirical mean (μ) and the empirical standard deviation (σ) were computed in the dB domain.

antennas for each fixed transmit antenna reinforced that the HF NVIS channel dynamically mixes polarization.

The relevance of metrics and statistics on spatial channel properties depends on the MIMO processing context. SNR statistics are sufficient to study diversity-mode performance in MIMO links since diversity mode takes advantage of SNR differences between different transmit-receive paths. The dynamic nature of SNR for each path was confirmed in the measurements. The histogram of each path ('Best Path' is antenna selection) is shown in Figure 9. Figure 10 shows the difference in SNR between the each individual path and the 'Best Path' due to antenna selection over the time interval of measurements. Note that each transmit-receive antenna pair observed a time when it is the strongest and also when it is the weakest. Further analysis of SNR data showed that, with a single antenna path, the expected change in SNR as a function of time is ± 0.64 dB/sec. If antenna selection was used, the expected change would have been ± 0.26 dB/sec, which means that antenna selection may slow down the variability of the channel quality by more than $2\times$. The least squares linear fit predicts that 50% correlation occurred at 5.88 seconds, which implies a Doppler frequency range of $0.03 - 0.25$ Hz using

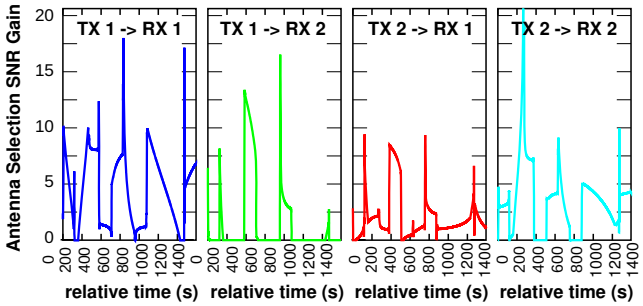

Fig. 10. Antenna selection SNR gain (compared to each single antenna pair).

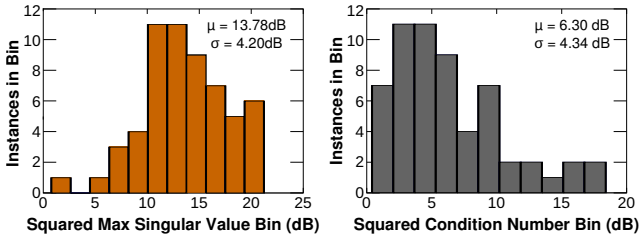

Fig. 11. Histogram of the narrowband channel matrix dominant normalized singular value and the condition number. The mean (μ) and standard deviation (σ) were computed in the dB domain.

equations (5.40.a)-(5.40.c) in [13]. Hence the measurements were captured in a benign HF NVIS Doppler channel [20].

The channel matrix condition number is a more suitable metric for spatial multiplexing since single-path SNR does not account for self-interference generated between paths. Figure 8 shows the condition number varied between 0.4 dB and 18.4 dB. With optimal precoding and parallel data transmitted in spatial multiplexing mode, one data stream would have had an SNR that was 0.4 dB to 18.4 dB stronger than the other stream. It is also helpful to calculate the expected SNR of the stronger stream. As shown in Section II, this is given by the dominant singular value normalized to the noise variance. The weaker stream SNR (in dB) is equal to the maximum normalized singular value (in dB) minus the condition number (in dB). Figure 11 shows the histogram for both the normalized singular value and condition number over all channel estimates.

The empirical spatial correlation matrix was computed as

$$\hat{\mathbf{Q}} = \begin{bmatrix} 1 & 0.46 & 0.69 & 0.98 \\ 0.46 & 1 & 0.89 & 0.55 \\ 0.69 & 0.89 & 1 & 0.76 \\ 0.98 & 0.55 & 0.76 & 1 \end{bmatrix} \tag{3}$$

with estimate bias removed. Note that because the frequency references of the transmit radios were not locked, phase ambiguity existed between the columns of the matrix. Although this did not change the condition number or the capacity of the channel matrix, it did change the correlation matrix. Hence, in (3) the measurements have been modified such that the paths TX1 $\rightarrow$ RX1 and TX2 $\rightarrow$ RX2 (which featured the same polarizations at the transmitter and receiver) had the same phase. If the phases between these two paths were random this would be equivalent to zeroing the terms that reflect the paths TX1 $\rightarrow$ RX2 and TX2 $\rightarrow$ RX1. Because this does not substantially impact capacity plots generated

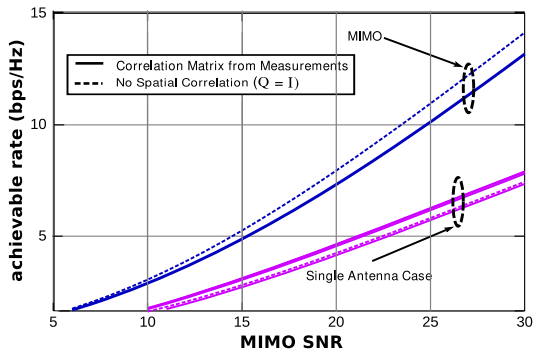

Fig. 12. Achievable rate as a function of MIMO SNR and spatial correlation. The companion paper elaborates on the performance of practical MIMO digital communications in these channels [1].

TABLE III. ADVANTAGE SUMMARY FOR HF NVIS MIMO WITH CROSS-POLARIZED ANTENNAS (COMPARED TO SINGLE-ANTENNA LINKS).

Property	MIMO Advantage	Source
Capacity	$\mathbf{1.8-2.3\times}$ **higher**	Figure 12.
TX Power	$\mathbf{2-9\times}$ **lower**	Figure 12.
Reliability	$\mathbf{3-4\times}$ **better**	Link SNR < 5 dB $3-4\times$ less often in Figure 8 and 9.

from the correlation matrices, the previous assumption of zero phase between the paths with equal polarization remains. Note also that initial calculation of $\mathbf{Q}$ yielded diagonal terms with different values. Correlation (covariance) matrix values are more useful when diagonal terms are the same (variance of the mean-subtracted distribution of each matrix element is the same). Intuitively, we expect this, but many factors (unequal efficiency of antennas) have shifted the variances.

Ergodic capacity reports the maximum achievable rate over the distribution of the channel noise at each receive antenna with a fixed variance. If each transmit antenna produces power P_t, each receive antenna experiences the same variance σ^2, and assuming the transmitter has no prior knowledge of channel information or spatial correlation, the capacity formula for narrowband MIMO channel matrix $\mathbf{H}$ is

$$C = \mathbb{E}_{\mathbf{H}}\left[\log_2\left(\det\left(\mathbf{I} + \frac{P_t \mathbf{H}\mathbf{H}^H}{\sigma_n^2}\right)\right)\right] \quad (4)$$

where $\mathbf{I}$ is the identity matrix and $\det(\cdot)$ takes the determinant.[1] The ergodic capacity plotted in Figure 12 represents the channel measurements through Monte Carlo simulations with the channel model parametrized by the spatial correlation matrix in (3). The MIMO capacity with power normalization is roughly twice the capacity of the single-antenna counterparts.

VI. CONCLUSION

This paper demonstrated the feasibility of HF MIMO for NVIS links with space-efficient cross-polarized, horizontally-oriented dipole antennas. The performance advantages of MIMO with diversity and spatial multiplexing, summarized in Table III, suggest that MIMO will be a game changing technology for tactical HF communications. Notably, MIMO allows the total transmit power to be reduced $2-9\times$ without sacrificing rate or reliability. This is attractive for operations with a minimal radiation footprint or for battery conservation. This paper also provided critical channel metrics to enable efficient simulation of cross-polarized HF NVIS MIMO channels.

[1]Ergodic capacity with spatial correlation knowledge uses different form.

ACKNOWLEDGMENTS

The authors would like to thank Dr. John Moniz and Dr. Jeffery Allen for their valuable feedback.

REFERENCES

[1] R. C. Daniels and S. W. Peters, "A new MIMO HF data link: Designing for high data rates and backwards compatibility," in *IEEE MILCOM*, 2013.

[2] M. B. Jorgenson, R. W. Johnson, R. Blocksome, R. W. Nelson, D. Harris, and G. Boesdorfer, "Implementation and on-air testing of a 64 kbps wideband HF data waveform," in *IEEE MILCOM*, 2010.

[3] D. Gesbert and J. Akhtar, "Breaking the barriers of Shannons capacity: An overview of MIMO wireless systems," *Signal Processing*, vol. 1, no. B2, p. B3, 2002.

[4] S. D. Gunashekar *et al.*, "Investigations into the feasibility of MIMO techniques within the HF band: Preliminary results," *Radio Science*, vol. 44, no. 1, 2009.

[5] P. M. Ndao, D. Lemur, Y. Erhel, and C. Brousseau, "Capacity estimation of MIMO ionospheric channels," in *Ionospheric Radio Systems and Techniques*, 2009.

[6] A. Forenza, R. W. Heath, Jr., S. G. Perlman, R. Van Der Laan, and J. Speck, "System and method for distributed input distributed output wireless communications," *US Patent Application 20080080631*, 2008.

[7] D. S. Baum, D. Gore, R. Nabar, S. Panchanathan, K. Hari, V. Erceg, and A. J. Paulraj, "Measurement and characterization of broadband MIMO fixed wireless channels at 2.5 GHz," in *IEEE Conference on Personal Wireless Communications*, 2000, pp. 203–206.

[8] R. C. Daniels and R. W. Heath, Jr., "Modeling ordered subcarrier SNR in MIMO-OFDM wireless links," *Physical Communication*, 2011.

[9] R. W. Heath, Jr. and A. J. Paulraj, "Switching between diversity and multiplexing in MIMO systems," *IEEE Transactions on Communications*, vol. 53, no. 6, pp. 962–968, 2005.

[10] W. Tranter, K. Shanmugan, T. S. Rappaport, and K. Kosbar, *Principles of communication systems simulation with wireless applications*. Prentice Hall Press, 2003.

[11] S. J. Burgess and N. E. Evans, "Characteristics of a mid-latitude NVIS HF radio channel," in *IEE National Conference on Antennas and Propagation*, 1999, pp. 101–104.

[12] L. Deneire, B. Gyselinckx, and M. Engels, "Training sequence versus cyclic prefix—A new look on single carrier communication," *IEEE Communications Letters*, vol. 5, no. 7, pp. 292–294, 2001.

[13] T. S. Rappaport, *Wireless communications: principles and practice*. Prentice Hall, 2002.

[14] C. A. Balanis, "Antenna theory and design," *John Wiley & Sons, Inc*, pp. 249–347, 1997.

[15] J. R. Wait, "The ancient and modern history of EM ground-wave propagation," *IEEE Antennas and Propagation Magazine*, vol. 40, no. 5, pp. 7–24, 1998.

[16] K. A. Norton, "The propagation of radio waves over the surface of the earth and in the upper atmosphere, part 1," *Proceedings of the IRE*, vol. 24, no. 10, pp. 1367–1387, 1936.

[17] G. Lane, "Signal-to-noise predictions using VOACAP – a users guide," *Rockwell Collins Inc., USA*, 2001.

[18] E. M. Vitucci, V. M. Kolmonen, V. Degli-Esposti, and P. Vainikainen, "Analysis of radio propagation in co- and cross-polarization in urban environment," in *IEEE International Symposium on Spread Spectrum Techniques and Applications*, vol. 8, 2008, pp. 277–281.

[19] D. Gesbert, H. Bolcskei, D. A. Gore, and A. J. Paulraj, "Outdoor MIMO wireless channels: Models and performance prediction," *IEEE Transactions on Communications*, vol. 50, no. 12, pp. 1926–1934, 2002.

[20] L. S. Wagner and J. A. Goldstein, "Channel spread parameters for the high-latitude, near-vertical-incidence-skywave HF channel: Correlation with geomagnetic activity." DTIC Document, Tech. Rep., 1995.